

MATERIALS SCIENCE

Highly crystalline and water-wettable benzobisthiazole-based covalent organic frameworks for enhanced photocatalytic hydrogen production

Wei Huang^{1,2,†}, Yongpan Hu^{1,2,†}, Zhengyuan Qin³, Yujin Ji^{1,2}, Xuan Zhao^{1,2}, Yunling Wu^{1,2}, Qing He^{1,2}, Youyong Li^{1,2,5}, Chunfeng Zhang³, Jun Lu^{4,*} and Yanguang Li^{1,2,5,*}

ABSTRACT

Two-dimensional covalent organic frameworks are promising for photocatalysis by virtue of their structural and functional diversity, but generally suffer from low activities relative to their inorganic competitors. To fulfill their full potential requires a rational tailoring of their structures at different scales as well as their surface properties. Herein, we demonstrate benzobisthiazole-based covalent organic frameworks as a superior photocatalyst for hydrogen production. The product features high crystallinity with ordered 2.5-nm-wide cylindrical mesopores and great water wettability. These structural advantages afford our polymeric photocatalyst with fast charge carrier dynamics as evidenced by a range of spectroscopic characterizations and excellent catalytic performances when suspended in solution or supported on melamine foams. Under visible-light irradiation, it enables efficient and stable hydrogen evolution with a production rate of $487 \mu\text{mol h}^{-1}$ (or a mass-specific rate of $48.7 \text{ mmol g}^{-1} \text{ h}^{-1}$)—far superior to the previous state of the art. We also demonstrate that hydrogen production can be stoichiometrically coupled with the oxidation conversion of biomass as exemplified by the conversion of furfuryl alcohol to 2-furaldehyde.

Keywords: covalent organic frameworks, photocatalysis, hydrogen evolution, benzobisthiazole, water-wettable

INTRODUCTION

The conversion of abundant solar energy into clean hydrogen fuels via photocatalytic water splitting is a promising pathway to accelerate our transition toward a sustainable energy future [1]. The key lies in the rational design of semiconductor photocatalysts ideally with broad light-absorption ranges, rapid charge separation and large accessible surface areas. Since the first report in 1972 [2], research attention has been predominantly focused on inorganic semiconductors such as TiO_2 , CdS and so on [3–6]. Polymeric photocatalysts, on the other hand, are unique for their Earth-abundant compositions and structural diversity, and therefore have tremendous potential to rival or even outperform their inorganic competitors [7–11]. By properly choosing the

building blocks and building sequences, their optoelectronic properties might be rationally tailored to demand. However, polymeric photocatalysts are far less explored.

Among a number of emerging polymeric candidates, ordered 2D covalent organic frameworks (2D-COFs) attract particular attention [12–17]. They are formed by the ordered stacking of molecular layers and usually possess periodic columnar π -arrays that can facilitate interlayer charge separation and transfer. Despite much exciting progress in this direction since the pioneering work by Lotsch and co-workers in 2014 [18], attainable photocatalytic performances of 2D-COFs remain very limited (mostly $<10 \text{ mmol g}^{-1} \text{ h}^{-1}$) [13]. This is mainly due to the large binding energy of

¹Institute of Functional Nano and Soft Materials (FUNSOM), Soochow University, Suzhou 215123, China;

²Jiangsu Key Laboratory for Advanced Negative Carbon Technologies, Soochow University, Suzhou 215123, China; ³National Laboratory of Solid State Microstructures, School of Physics, and Collaborative Innovation Center for Advanced Microstructures, Nanjing University, Nanjing 210093, China; ⁴College of Chemical and Biological Engineering, Zhejiang University, Hangzhou 310027, China and ⁵Macao Institute of Materials Science and Engineering (MIMSE), MUST-SUDA Joint Research Center for Advanced Functional Materials, Macau University of Science and Technology, Macau, China

*Corresponding authors. E-mails: yanguang@suda.edu.cn; junzoelu@zju.edu.cn
†Equally contributed to this work.

Received 7 June 2022; Revised 20 July 2022; Accepted 10 August 2022

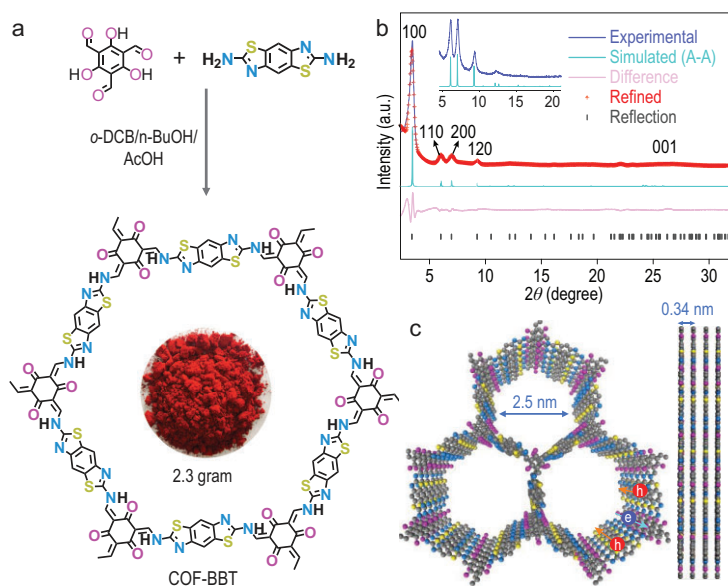


Figure 1. Synthesis and molecular topology of COF-BBT. (a) Schematic synthetic procedure toward COF-BBT; the inset illustrates the powdery product from a single reaction batch; (b) experimental and simulated XRD patterns of COF-BBT together with its Rietveld refinement result; (c) schematic structure of COF-BBT viewed from the top and the side.

their Frenkel excitons and consequent problematic exciton dissociation [8,19]; the hydrophobic nature of their π -conjugated aromatic backbones often causes their large inner porosity to be inaccessible to water [20,21]. In order to tackle the above challenges, synthetic and structural modifications are desired to promote the structural crystallinity and polarity of 2D-COFs.

Incorporating heteroatom-rich moieties into the organic frameworks of 2D-COFs can effectively increase their water wettability, expose abundant inner surface sites and facilitate exciton dissociation [8,22,23]. Here, we demonstrate the critical roles of benzobisthiazole (BBT) units in improving the photocatalytic properties of 2D-COFs: it is a nitrogen- and sulfur-containing aromatic heterocycle that may increase the product surface wettability; its rigid and planar configuration would promote structural crystallinity and enhance the intralayer electron delocalization and interlayer π - π stacking. Thanks to its high crystallinity and great water wettability, the resulting BBT-containing 2D-COF exhibits outstanding photocatalytic performance.

RESULTS AND DISCUSSION

Synthesis and characterizations of benzobisthiazole-based 2D-COF

Figure 1a schematically illustrates the synthesis of the benzobisthiazole-based 2D-COF

(COF-BBT) from the condensation between 2,6-diaminebenzobisthiazole (DABBT) and 1,3,5-triformylphloroglucinol (TFP) in the presence of acetic acid as the catalyst. In Schiff-base reactions, the acid catalyst is known to favor the reversible cross-linking of individual building blocks that provides a self-correction mechanism to gradually heal defects and form ordered structures over time [24]. Here, the low oxygen reactivity of primary amines in DABBT (owing to the electron-deficient nature of benzobisthiazole) allows the reaction to proceed without the inert gas protection and renders our synthetic procedure significantly more straightforward and scalable compared to the syntheses of other similar COF materials [25]. For control experiments, we also prepared an amorphous benzobisthiazole-based covalent organic polymer (COP-BBT) in the absence of acetic acid, as well as a model molecule from the reaction of TFP and 2-aminobenzothiazole.

The cross-linked molecular structures of COF-BBT and COP-BBT were first verified using Fourier-transform infrared (FTIR) spectroscopy, nuclear magnetic resonance (NMR) spectroscopy and X-ray photoelectron spectroscopy (XPS). As shown in Supplementary Fig. S1, the absence of the stretching vibrations of aldehyde ($-\text{CH}=\text{O}$) at 1636 cm^{-1} or amine ($-\text{NH}_2$) at $3392\text{--}3276\text{ cm}^{-1}$ in the FTIR spectra of COF-BBT and COP-BBT suggests the complete condensation of the starting monomers. Two new peaks instead emerge at 1602 and 1565 cm^{-1} , corresponding to the ketone ($\text{C}=\text{O}$) and $\text{C}=\text{C}$ bonding, respectively, of the β -ketoenamine linkage. Their solid-state ^{13}C NMR spectra further reveal the presence of the ketone carbon at 184 ppm (Supplementary Fig. S2). Moreover, the N 1s XPS spectrum of COF-BBT exhibits two intensive peaks at 399.0 and 400.6 eV that can be ascribed to the $\text{C}-\text{NH}$ bond in the enamine and the $\text{C}=\text{N}$ bond in the BBT units, respectively (Supplementary Fig. S3). Their spectral fingerprints are also identical to those of the model molecule. All these results unambiguously indicate the formation of β -ketoenamine linkages and the incorporation of BBT units into the organic skeletons. The X-ray diffraction (XRD) pattern of COF-BBT exhibits intense diffraction peaks that can be perfectly simulated by the eclipsed (A-A) stacking of molecular layers (Fig. 1b and Supplementary Fig. S4). The strongest peak at $2\theta = 3.5^\circ$ is assignable to the (100) diffraction and evidences the long-range structural ordering with a periodic pore-to-pore distance of 25.2 \AA . The interlayer distance of COF-BBT is estimated to be 3.4 \AA from its (001) diffraction at $2\theta = 26.3^\circ$. Compared to the staggered (A-B) configuration, such a π - π cofacial

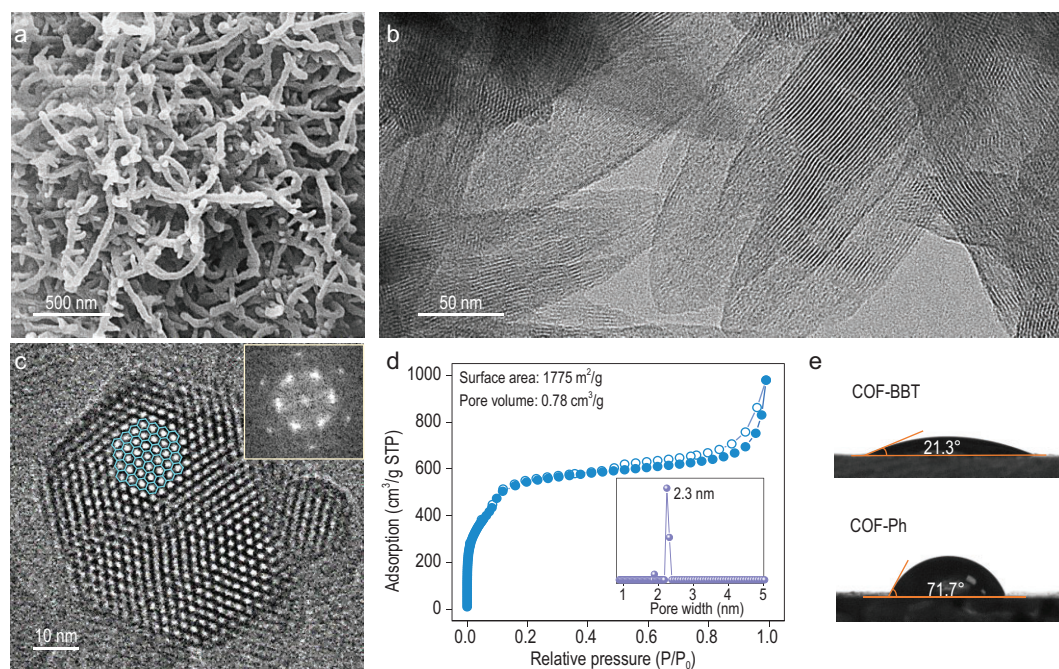


Figure 2. Nanostructure and surface property of COF-BBT. (a) SEM image and (b and c) TEM images of COF-BBT nanofibers; the inset of (c) is the fast Fourier-transform (FTT) pattern of the hexagonal mesopore arrangement at the nanofiber cross section; (d) N_2 isotherm of COF-BBT; the inset shows the corresponding pore size distribution curve; (e) water contact angles of COF-BBT and COF-Ph.

assembly would facilitate the interlayer charge separation and transfer during photocatalysis (Fig. 1c) [26]. By contrast, the XRD of COP-BBT is largely featureless and thereby attests to its amorphous nature despite the same building units as COF-BBT (Supplementary Fig. S5).

Scanning electron microscopy (SEM) imaging of COF-BBT shows that it consists of nanofibers of ~ 100 nm in diameter and >1 μm in length (Fig. 2a). Transmission electron microscopy (TEM) analysis corroborates the high structural crystallinity. Its 1D mesoporous channels are observed to extend in parallel along the nanofiber long-axis, which indicates that individual nanofibers are formed from the stacking layers along the [001] direction (Fig. 2b). The TEM image of a nanofiber cross section clearly unveils the hexagonal arrangement of these 1D channels (Fig. 2c). Their width is measured to be ~ 2.5 nm, in good agreement with above XRD analysis. N_2 sorption measurement shows that COF-BBT has a large surface area of $1775\text{ m}^2\text{ g}^{-1}$ and a total pore volume of $0.78\text{ cm}^3\text{ g}^{-1}$ (Fig. 2d). Its corresponding pore size distribution curve exhibits a sharp peak at 2.3 nm (Fig. 2d, inset). By contrast, COP-BBT shows a similar fibrous morphology but lacks long-range structural ordering under TEM (Supplementary Fig. S6). It has a considerably smaller surface area of $420\text{ m}^2\text{ g}^{-1}$ and broad pore size distribution

owing to its disordered molecular frameworks (Supplementary Fig. S7).

Further, it is worth highlighting that our samples have excellent chemical and thermal stability (Supplementary Figs S8 and S9) and great surface wettability essential to aqueous photocatalysis. Typical polymeric photocatalysts have water contact angles in the range of 60 – 110° [20]. Here, thin films of our COF-BBT and COP-BBT are measured to have a small water contact angle of 21° and 28° , respectively (Fig. 2e and Supplementary Figs S10 and S11). This is due to the incorporation of heteroatom-rich BBT units, giving rise to the increased structural polarity and water affinity. As side evidence, we also prepared a 2D-COF (COF-Ph) containing benzene units instead of BBT following a previous publication [27]. Its structural characterizations are summarized in Supplementary Fig. S12. COF-Ph thin film exhibits a relatively large water contact angle of 72° . Moreover, water sorption isotherms also corroborate the much-improved surface wettability of COF-BBT ($694\text{ cm}^3\text{ g}^{-1}$ or 56 wt% at standard temperature and pressure (STP)) and COP-BBT ($452\text{ cm}^3\text{ g}^{-1}$ or 36 wt% at STP) compared to COF-Ph ($183\text{ cm}^3\text{ g}^{-1}$ or 15 wt% at STP) (Supplementary Fig. S13).

The optical properties and electronic structures of our samples were next investigated. The ultraviolet-visible (UV-Vis) diffuse reflectance

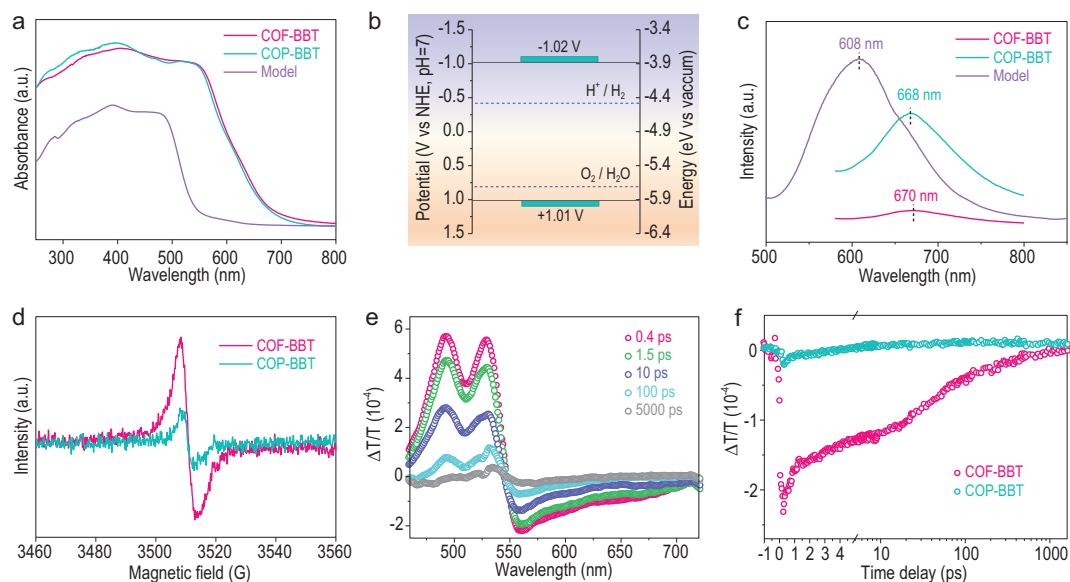


Figure 3. Optical properties and charge dynamics analysis. (a) UV–Vis diffuse reflectance spectra of COF-BBT, COP-BBT and the model molecule; (b) HOMO and LUMO positions of COF-BBT together with the theoretical potentials of hydrogen evolution and water oxidation; (c) steady-state PL emission spectra of COF-BBT, COP-BBT and the model molecule under 400-nm excitation; (d) EPR spectra of COF-BBT and COP-BBT under visible-light irradiation ($\lambda > 420$ nm); (e) TA spectra of COF-BBT at different decay times under 525-nm excitation; (f) TA traces of ESA signals from COF-BBT and COP-BBT probed at 560 and 625 nm, respectively.

spectra of COF-BBT and COP-BBT have an adsorption edge at ~ 700 nm and a tail extended up to ~ 800 nm (Fig. 3a). Corresponding Tauc plot analysis suggests a narrow optical band gap of ~ 2.0 eV for both of them (Supplementary Fig. S14). Mott-Schottky analysis of COF-BBT reveals that its lowest unoccupied molecular orbital (LUMO) locates at -1.02 V versus normal hydrogen electrode at pH 7 (Supplementary Fig. S15). The highest occupied molecular orbital (HOMO) is accordingly determined to be at $+1.01$ V based on its optical band gap as depicted in Fig. 3b. The band structure of COF-BBT is also confirmed using ultraviolet photoelectron spectroscopy and cyclic voltammogram analyses (Supplementary Figs S16 and S17). Density functional theory (DFT) simulations show that the electron density of HOMO is centered on the BBT unit, whereas that of LUMO mainly distributes over the keto unit (Supplementary Fig. S18). Their uneven distributions imply the possible electron transfer from BBT to keto upon light excitation.

High structural crystallinity is beneficial to the charge separation and transport during photocatalysis. In light of their very similar chemical compositions, surface wettability and optical properties, COF-BBT and COP-BBT here form an ideal couple for studying the effect of structural crystallinity on their charge carrier dynamics. Figure 3c compares their steady-state photoluminescence (PL) emission spectra as well as that of the model

molecule. Powdery COF-BBT exhibits significantly suppressed PL emission compared to those of COP-BBT and the model molecule. The average fluorescence lifetimes of COF-BBT and COP-BBT are determined to be 296 and 248 ps, respectively (Supplementary Fig. S19). The electron paramagnetic resonance (EPR) spectrum of COF-BBT exhibits a three-times more intense signal relative to that of COP-BBT, indicative of the enhanced exciton dissociation thanks to its ordered molecular frameworks (Fig. 3d) [28,29]. COF-BBT thin film grown on a fluorine-doped tin oxide electrode also exhibits substantially enhanced photocurrent density in solution compared with COP-BBT and the model molecule (Supplementary Fig. S20).

Moreover, we performed ultrafast transient absorption (TA) spectroscopic measurements to study the dynamics of photo-excited carriers. The transmittance (T) rather than other absorbance of the samples was recorded using our experimental set-up. As shown in Fig. 3e and Supplementary Fig. S21, the ground-state bleaching signals ($\Delta T/T > 0$) in the range of 450–550 nm are observed for both COF-BBT and COP-BBT [30]. Simultaneously, the excited-state absorption (ESA) signals appear in the longer wavelength range upon optical pump, which is likely caused by the primary charge-transfer excitations. Notably, the ESA signal is more pronounced in COF-BBT and persists for a longer timescale than that in amorphous

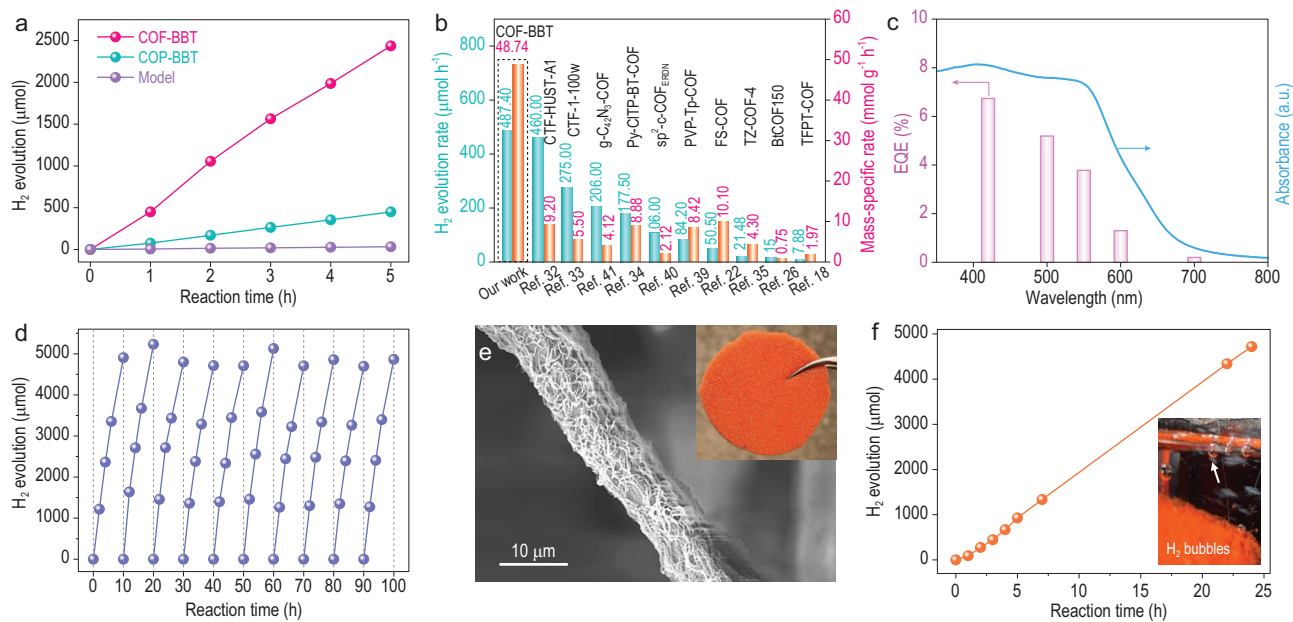


Figure 4. Photocatalytic H₂ production on COF-BBT. (a) Photocatalytic H₂ production curves of COF-BBT, COP-BBT and the model molecule; (b) comparison on the photocatalytic H₂ evolution rate and the mass-specific H₂ evolution rate of COF-BBT and previous states of the art from literature; (c) wavelength-dependent EQE values of COF-BBT together with its UV-Vis spectra; (d) consecutive cycles of photocatalytic H₂ production on COF-BBT for ≤100 h; (e) digital image and SEM image of COF-BBT loaded melamine foam; (f) photocatalytic H₂ production curve of COF-BBT loaded melamine foam; the inset shows H₂ bubbles evolving from the foam upon the light irradiation.

COP-BBT (Fig. 3f and Supplementary Fig. S22). The excited-state lifetime of the former is estimated to be ~20 ps, which is 3.3 times longer than that of the latter (6 ps). This possibly reflects the fewer structural defects in the ordered framework that effectively retard the charge trapping and recombination [31]. All the above spectroscopic characterizations unambiguously corroborate that the high structural crystallinity of COF-BBT affords it with much enhanced charge carrier dynamics.

Photocatalytic H₂ production

For the next step, we assessed the photocatalytic performance of COF-BBT for hydrogen production under the illumination of a 300-W Xe lamp equipped with a UV-cut-off filter (>420 nm). As with other COF-based photocatalysis, ascorbic acid was introduced in our experiments as the sacrificial electron donor. An optimized 3 wt% of Pt nanoparticles were *in situ* photo-deposited as the cocatalyst (Supplementary Fig. S23). Supplementary Fig. S24 illustrates the high-resolution TEM image of Pt-deposited COF-BBT. X-ray absorption (XAS) analysis at the Pt L3-edge discloses the non-zero valence state of Pt and the prevailing Pt–O bonding likely resulting from the interaction between Pt and oxygen atoms of the keto nodes (Supplementary

Fig. S25). The actual Pt content is measured to be 2.4 wt% by inductively coupled plasma (ICP) analysis. Figure 4a depicts the time-dependent hydrogen evolution curve of COF-BBT (10 mg) for the first 5 h; 450 μmol of H₂ is produced during the first hour. Its amount accumulates linearly with the reaction time and reaches 2437 μmol at the end of the 5 h of irradiation. This translates into an average hydrogen production rate of 487 μmol h⁻¹ or an average mass-specific rate of 48.7 mmol g⁻¹ h⁻¹—both are among the highest values ever reported for COF-based photocatalysis to date (Fig. 4b and Supplementary Table S1) [32–36]. Worth highlighting is that its mass-specific rate is more than four times larger than the previous COF-based state-of-the-art sulfone-containing 2D-COF developed by Cooper and co-workers [22]. We are aware that higher mass-specific rates were reported for some organic semiconductors beyond COFs, but they were attained by either adopting extremely low catalyst masses or using organic co-solvents [37,38]. Control experiments show that no H₂ is produced in the absence of light, a photocatalyst or the sacrificial electron donor under otherwise identical conditions. Further, the model molecule has a negligible photocatalytic activity; amorphous COP-BBT was measured to have an average mass-specific H₂ production rate of 9.0 mmol g⁻¹ h⁻¹ during the 5 h of photocatalysis. The observed difference in

photocatalytic activities is in line with the above analysis of charge carrier dynamics and again highlights the advantage of extended structural crystallinity and surface wettability. We note that once the mesopores of COF-BBT are blocked by polyethylene glycol, its photocatalytic activity significantly decreases (Supplementary Fig. S26). Figure 4c shows the wavelength-dependent external quantum efficiency (EQE) of COF-BBT. A high value of 6.8% is measured at 420 nm, which is superior to most other COF-based photocatalysts available so far (Supplementary Table S1) [39–41]. Impressively, our COF-BBT is photoactive even in the longer wavelength range of the visible spectrum and attains a remarkable EQE value of 0.2% at 700 nm. The EQE value of organic photocatalysts is generally limited (<5%) due to the formation of strongly bound Frenkel excitons [42]. This can be compensated by their broad light absorption. By contrast, inorganic semiconductors (e.g. TiO₂) and C₃N₄ may exhibit higher EQE values in the near-UV region, but usually have negligible absorption at longer wavelengths (>550 nm) that leads to overall lower photocatalytic activities (Supplementary Fig. S27).

Stability of COF-BBT was then evaluated via cycling experiments. As shown in Fig. 4d, there is no activity loss for 10 cycles and a total reaction time of 100 h. This is, however, far from the possible lifetime of our COF-BBT. After the long-term stability test, recollected COF-BBT was subjected to FTIR, UV-Vis, XRD, XPS and TEM characterizations (Supplementary Figs S3 and S28). No obvious structural change is noted, thereby attesting to its great stability. ICP analysis of the solution reveals no discernible increase in the sulfur concentration after photocatalysis, further ruling out possible material degradation (Supplementary Table S2).

We made a few more explorations. Pt cocatalyst here serves as the active site to receive photogenerated electrons from COF-BBT and catalyse hydrogen evolution on the surface. Despite the predominant use of Pt cocatalyst in polymeric photocatalysis, it would be highly tempting to search for non-precious-metal-based alternatives. To this end, we chemically deposited 3 wt% Ni, Co and Cu on COF-BBT (Supplementary Fig. S29) [43]. When evaluated under identical conditions, Ni-loaded COF-BBT is measured to be the most active with an average hydrogen production rate of 7.7 $\mu\text{mol h}^{-1}$ or a mass-specific rate of 770 $\mu\text{mol g}^{-1} \text{h}^{-1}$ (Supplementary Fig. S30). Although ~ 60 times lower than those of Pt-loaded COF-BBT, this rate is roughly comparable to the state of the art using non-precious-metal-based co-catalysts [44,45].

For practical applications, it is often desired to load powdery photocatalysts onto high-surface-area and photo-inactive supports to facilitate the catalyst recycling [46–48]. We here demonstrate that our COF-BBT can directly grow on porous melamine foams. Successful catalyst loading is reflected from the evident color change of the support from white to orange (Fig. 4e and Supplementary Fig. S31). These catalyst-loaded foams can be readily cut into a variety of shapes and thicknesses as needed for photocatalytic applications. The COF-BBT content is typically controlled to be ~ 3 wt%. SEM examination reveals that at such a dilute catalyst concentration, micrometer-long fibers of COF-BBT tightly wrap around the foam skeleton and densely cover the substrate. When immersed into the solution of ascorbic acid and *in situ* photo-deposited with Pt, the catalyst-loaded melamine foam (in a circular shape with 3 cm in diameter and 3 mm in thickness) enables stable H₂ production under visible-light irradiation, giving rise to a total of 4717 μmol of H₂ over 24 h (Fig. 4f). This translates into an average H₂ production rate of 28 $\mu\text{mol cm}^{-2} \text{h}^{-1}$. At the end of the reaction, the catalyst can be simply retrieved by taking out the melamine foam from the solution. No visible catalyst falling off is observed and the surface texture of the foam remains (Supplementary Fig. S32).

Coupling of H₂ production and the selective oxidation of biomass

Another obstacle in the practical applications of COF-based or, more generally, polymer-based photocatalysts is the common use of sacrificial electron donors [8]. Even though the band structure of COF-BBT is analysed to straddle the potentials of hydrogen evolution and water oxidation, no O₂ can be measured experimentally in the absence of ascorbic acid with or without co-catalysts (e.g. CoO_x). This is probably because the water oxidation overpotential (calculated to be ~ 190 mV) is too small to effectively drive this demanding half reaction [8]. One solution is to pursue Z-scheme photocatalysis by integrating two different semiconductor materials with proper band offset for separate half reactions [49]. Another strategy is to integrate hydrogen evolution with the oxidation transformation of organic substrates that can take place under milder conditions and yield higher-valued products than O₂ [50–52].

In our experiments, we attempted to substitute ascorbic acid with furfuryl alcohol (a common biomass-derived chemical) to scavenge photogenerated holes. During the reaction, furfuryl alcohol is selectively oxidized to 2-furaldehyde, which is an important chemical intermediate for the plastic

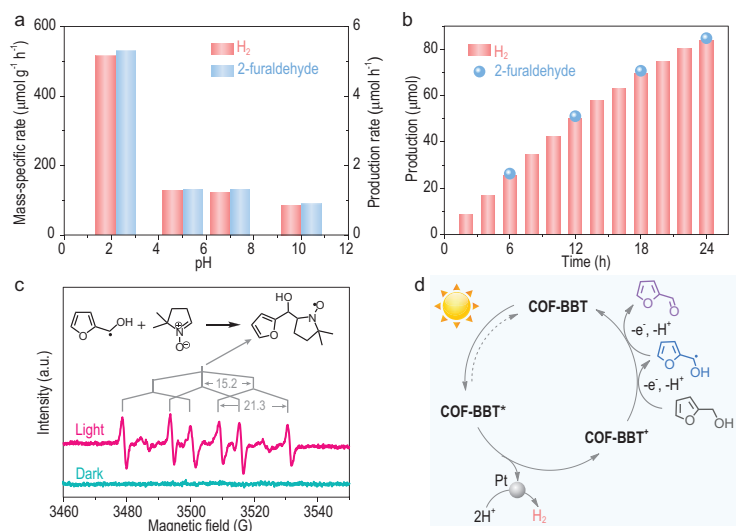


Figure 5. Photocatalytic H₂ production coupled with the selective oxidation of furfuryl alcohol of COF-BBT. (a) pH-dependent photocatalytic activities for the coupled reaction; (b) photocatalytic co-production of H₂ and 2-furaldehyde at pH = 2.2 over a long-term reaction period; (c) *in situ* EPR analysis during the photocatalytic oxidation of furfuryl alcohol in the presence of DMPO in the dark or light; (d) proposed reaction mechanism.

and pharmaceutical industry [53]. The reaction shows interesting pH dependence (Fig. 5a). The activity is measured to be the highest in pH = 2.2 solution (adjusted with the addition of HClO₄). The H₂ and 2-furaldehyde products are found to be stoichiometric and their average mass-specific activities reach $530 \mu\text{mol g}^{-1} \text{h}^{-1}$. Further lowering the solution pH to <2 causes catalyst instability, while increasing the solution pH to >4 noticeably compromises the activity. Control experiments demonstrate the vital roles of different reaction components (Supplementary Fig. S33). Even though the optimal H₂ production rate measured here is ~ 100 times slower than that measured in the presence of ascorbic acid (presumably due to the different hole-scavenging kinetics of furfuryl alcohol and ascorbic acid), the study here suggests that the proposed approach is viable for the first time for polymeric photocatalysts (excluding C₃N₄). Future improvement can be made by adjusting the redox potential of the organic substrate and optimizing its interaction with the photocatalyst.

We further investigated the long-term stability of the photocatalytic conversion under the optimal conditions. As shown in Fig. 5b, an approximately linear increase in H₂ is observed up to 24 h under visible-light irradiation, producing a total amount of $\sim 84 \mu\text{mol H}_2$. During the reaction, the amount of 2-furaldehyde accumulated in the solution was examined every 6 h and was analysed to be generally consistent with the hydrogen evolution curve. It supports that the two half reactions are close to stoi-

chiometry even over a long reaction period and indicates high reaction selectivity and no over-oxidation of 2-furaldehyde beyond two electrons.

Finally, in order to understand how furfuryl alcohol is oxidized, an *in situ* EPR experiment was carried out during photocatalysis using 5,5-dimethyl-1-pyrroline-N-oxide (DMPO) as the radical trapping agent. No EPR signal was observed in the dark, while a pronounced set of EPR signals were observed in the light, corresponding to the formation of hydroxymethyl carbon radical during photocatalysis that becomes trapped by DMPO (Fig. 5c) [54,55]. It evidences that the oxidation of furfuryl alcohol to 2-furaldehyde involves a free-radical intermediate. Based on the above results, a schematic cycle mechanism is proposed for photocatalytic hydrogen evolution and furfuryl alcohol oxidation as shown in Fig. 5d.

CONCLUSION

In summary, we demonstrated BBT-COF as an efficient and robust photocatalyst for hydrogen production. The material featured great structural crystallinity and water wettability owing to the incorporation of rigid and polar BBT units. BBT-COF exhibited fast charge carrier dynamics as evidenced by a range of spectroscopic characterizations and excellent photocatalytic performances when either suspended in solution or supported on melamine foams. Most impressively, a mass-specific hydrogen production rate of $48.7 \text{ mmol g}^{-1} \text{h}^{-1}$ and EQE of 6.8% at 420 nm were measured in the presence of sacrificial electron donors, which is superior to the previous state of the art. Further, the photocatalytic hydrogen production could be coupled with the oxidation of furfuryl alcohol to 2-furaldehyde at stoichiometry. Our study here highlights the tremendous potential of COF-based photocatalysis to rival or even outperform the so far predominant inorganic-based photocatalysis.

SUPPLEMENTARY DATA

Supplementary data are available at [NSR](#) online.

ACKNOWLEDGEMENTS

We thank Ying Shao and Dr. Zhangxiong Wu for the assistance with water sorption experiments, and Chen Cheng and Dr. Liang Zhang for the assistance with XAS experiments.

FUNDING

This work was supported by the National Natural Science Foundation of China (22002100 and U2002213), the

Science and Technology Development Fund Macau SAR (0077/2021/A2), the Natural Science Foundation of Jiangsu Province (BK20220027), the Priority Academic Program Development of Jiangsu Higher Education Institutions and the Collaborative Innovation Center of Suzhou Nano Science and Technology.

AUTHOR CONTRIBUTIONS

Y.G.L. conceived and directed the study; W.H. performed the material synthesis and photocatalytic measurements; Y.H. conducted the FTIR and XRD characterizations; Z.Q. and C.Z. collected and analysed the TA spectroscopy data; Y.J. and Y.Y.L. carried out DFT simulations; X.Z. and Y.Y. conducted the SEM and TEM characterizations; Y.W. performed the N₂ absorption/desorption measurements. W.H., J.L. and Y.G.L. co-wrote the manuscript with contributions from all the authors.

Conflict of interest statement. None declared.

REFERENCES

- Tachibana Y, Vayssieres L and Durrant JR. Artificial photosynthesis for solar water-splitting. *Nat Photon* 2012; **6**: 511–8.
- Fujishima A and Honda K. Electrochemical photolysis of water at a semiconductor electrode. *Nature* 1972; **238**: 37–8.
- Hisatomi T, Kubota J and Domen K. Recent advances in semiconductors for photocatalytic and photoelectrochemical water splitting. *Chem Soc Rev* 2014; **43**: 7520–35.
- Cheng L, Xiang Q and Liao Y *et al.* CdS-based photocatalysts. *Energy Environ Sci* 2018; **11**: 1362–91.
- Sivula K and Van De Krol R. Semiconducting materials for photoelectrochemical energy conversion. *Nat Rev Mater* 2016; **1**: 15010.
- Chen S, Takata T and Domen K. Particulate photocatalysts for overall water splitting. *Nat Rev Mater* 2017; **2**: 17050.
- Dai C and Liu B. Conjugated polymers for visible-light-driven photocatalysis. *Energy Environ Sci* 2020; **13**: 24–52.
- Wang Y, Vogel A and Sachs M *et al.* Current understanding and challenges of solar-driven hydrogen generation using polymeric photocatalysts. *Nat Energy* 2019; **4**: 746–60.
- Zhao C, Chen Z and Shi R *et al.* Recent advances in conjugated polymers for visible-light-driven water splitting. *Adv Mater* 2020; **32**: 1907296.
- Zhang G, Lan ZA and Wang X. Conjugated polymers: catalysts for photocatalytic hydrogen evolution. *Angew Chem Int Ed* 2016; **55**: 15712–27.
- Zhang T, Xing GL and Chen WB *et al.* Porous organic polymers: a promising platform for efficient photocatalysis. *Mater Chem Front* 2020; **4**: 332–53.
- Medina DD, Sick T and Bein T. Photoactive and conducting covalent organic frameworks. *Adv Energy Mater* 2017; **7**: 1700387.
- Huang W, Luo W and Li YG. Two-dimensional semiconducting covalent organic frameworks for photocatalytic solar fuel production. *Mater Today* 2020; **40**: 160–72.
- Chen X, Geng K and Liu R *et al.* Covalent organic frameworks: chemical approaches to designer structures and built-in functions. *Angew Chem Int Ed* 2020; **59**: 5050–91.
- Jakowetz AC, Hinrichsen TF and Ascherl L *et al.* Excited-state dynamics in fully conjugated 2D covalent organic frameworks. *J Am Chem Soc* 2019; **141**: 11565–71.
- Li YS, Chen WB and Xing GL *et al.* New synthetic strategies toward covalent organic frameworks. *Chem Soc Rev* 2020; **49**: 2852–68.
- Li YS, Chen Q and Xu TT *et al.* De novo design and facile synthesis of 2D covalent organic frameworks: a two-in-one strategy. *J Am Chem Soc* 2019; **141**: 13822–8.
- Stegbauer L, Schwinghammer K and Lotsch BV. A hydrazone-based covalent organic framework for photocatalytic hydrogen production. *Chem Sci* 2014; **5**: 2789–93.
- Zhu XY, Yang Q and Muntwiler M. Charge-transfer excitons at organic semiconductor surfaces and interfaces. *Acc Chem Res* 2009; **42**: 1779–87.
- Dawson R, Laybourn A and Clowes R *et al.* Functionalized conjugated microporous polymers. *Macromolecules* 2009; **42**: 8809–16.
- Wang X, Chen B and Dong W *et al.* Hydrophilicity controlled conjugated microporous polymers for enhanced visible-light-driven photocatalytic H₂ evolution. *Macromol Rapid Commun* 2019; **40**: 1800494.
- Wang X, Chen L and Chong SY *et al.* Sulfone-containing covalent organic frameworks for photocatalytic hydrogen evolution from water. *Nat Chem* 2018; **10**: 1180–9.
- Chen WB, Yang ZF and Xie Z *et al.* Benzothiadiazole functionalized D-A type covalent organic frameworks for effective photocatalytic reduction of aqueous chromium(VI). *J Mater Chem A* 2019; **7**: 998–1004.
- Haase F and Lotsch BV. Solving the COF trilemma: towards crystalline, stable and functional covalent organic frameworks. *Chem Soc Rev* 2020; **49**: 8469–500.
- Lohse MS and Bein T. Covalent organic frameworks: structures, synthesis, and applications. *Adv Funct Mater* 2018; **28**: 1705553.
- Ghosh S, Nakada A and Springer MA *et al.* Identification of prime factors to maximize the photocatalytic hydrogen evolution of covalent organic frameworks. *J Am Chem Soc* 2020; **142**: 9752–62.
- Kandambeth S, Mallick A and Lukose B *et al.* Construction of crystalline 2D covalent organic frameworks with remarkable chemical (acid/base) stability via a combined reversible and irreversible route. *J Am Chem Soc* 2012; **134**: 19524–7.
- Shiraishi Y, Takii T and Hagi T *et al.* Resorcinol–formaldehyde resins as metal-free semiconductor photocatalysts for solar-to-hydrogen peroxide energy conversion. *Nat Mater* 2019; **18**: 985–93.
- Wei Z, Liu M and Zhang Z *et al.* Efficient visible-light-driven selective oxygen reduction to hydrogen peroxide by oxygen-enriched graphitic carbon nitride polymers. *Energy Environ Sci* 2018; **11**: 2581–9.
- Berera R, van Grondelle R and Kennis JT. Ultrafast transient absorption spectroscopy: principles and application to photosynthetic systems. *Photosynth Res* 2009; **101**: 105–18.

31. Yang S, Hu W and Zhang X *et al.* 2D covalent organic frameworks as intrinsic photocatalysts for visible light-driven CO₂ reduction. *J Am Chem Soc* 2018; **140**: 14614–8.
32. Zhang S, Cheng G and Guo L *et al.* Strong-base-assisted synthesis of a crystalline covalent triazine framework with high hydrophilicity via benzylamine monomer for photocatalytic water splitting. *Angew Chem Int Ed* 2020; **59**: 6007–14.
33. Xie J, Shevlin SA and Ruan Q *et al.* Efficient visible light-driven water oxidation and proton reduction by an ordered covalent triazine-based framework. *Energy Environ Sci* 2018; **11**: 1617–24.
34. Chen W, Wang L and Mo D *et al.* Modulating benzothiadiazole-based covalent organic frameworks via halogenation for enhanced photocatalytic water splitting. *Angew Chem Int Ed* 2020; **59**: 16902–9.
35. Wang K, Jia Z and Bai Y *et al.* Synthesis of stable thiazole-linked covalent organic frameworks via a multicomponent reaction. *J Am Chem Soc* 2020; **142**: 11131–8.
36. Li C, Liu J and Li H *et al.* Covalent organic frameworks with high quantum efficiency in sacrificial photocatalytic hydrogen evolution. *Nat Commun* 2022; **13**: 2357.
37. Kosco J, Bidwell M and Cha H *et al.* Enhanced photocatalytic hydrogen evolution from organic semiconductor heterojunction nanoparticles. *Nat Mater* 2020; **19**: 559–65.
38. Cheng JZ, Liu LL and Liao GF *et al.* Achieving an unprecedented hydrogen evolution rate by solvent-exfoliated CPP-based photocatalysts. *J Mater Chem A* 2020; **8**: 5890–9.
39. Ming J, Liu A and Zhao J *et al.* Hot π -electron tunneling of metal–insulator–COF nanostructures for efficient hydrogen production. *Angew Chem Int Ed* 2019; **58**: 18290–4.
40. Jin E, Lan Z and Jiang Q *et al.* 2D sp² carbon-conjugated covalent organic frameworks for photocatalytic hydrogen production from water. *Chem* 2019; **5**: 1632–47.
41. Bi S, Yang C and Zhang W *et al.* Two-dimensional semiconducting covalent organic frameworks via condensation at arylmethyl carbon atoms. *Nat Commun* 2019; **10**: 2467.
42. Kosco J, Moruzzi F and Willner B *et al.* Photocatalysts based on organic semiconductors with tunable energy levels for solar fuel applications. *Adv Energy Mater* 2020; **10**: 2001935.
43. Tran PD, Xi LF and Batabyal SK *et al.* Enhancing the photocatalytic efficiency of TiO₂ nanopowders for H₂ production by using non-noble transition metal co-catalysts. *Phys Chem Chem Phys* 2012; **14**: 11596–9.
44. Banerjee T, Haase F and Savasci G *et al.* Single-site photocatalytic H₂ evolution from covalent organic frameworks with molecular cobaloxime co-catalysts. *J Am Chem Soc* 2017; **139**: 16228–34.
45. Diaz L, Rodriguez VD and Gonzalez-Rodriguez M *et al.* M/TiO₂ (M = Fe, Co, Ni, Cu, Zn) catalysts for photocatalytic hydrogen production under UV and visible light irradiation. *Inorg Chem Front* 2021; **8**: 3491–500.
46. Huang W, Ma BC and Wang D *et al.* A fixed-bed photoreactor using conjugated nanoporous polymer-coated glass fibers for visible light-promoted continuous photoredox reactions. *J Mater Chem A* 2017; **5**: 3792–7.
47. Hisatomi T and Domen K. Reaction systems for solar hydrogen production via water splitting with particulate semiconductor photocatalysts. *Nat Catal* 2019; **2**: 387–99.
48. Spasiano D, Marotta R and Malato S *et al.* Solar photocatalysis: materials, reactors, some commercial, and pre-industrialized applications—a comprehensive approach. *Appl Catal B* 2015; **170**: 90–123.
49. Wang L, Zheng XS and Chen L *et al.* Van der waals heterostructures comprised of ultrathin polymer nanosheets for efficient Z-scheme overall water splitting. *Angew Chem Int Ed* 2018; **57**: 3454–8.
50. Kampouri S and Stylianou KC. Dual-functional photocatalysis for simultaneous hydrogen production and oxidation of organic substances. *ACS Catal* 2019; **9**: 4247–70.
51. Han G, Jin YH and Burgess RA *et al.* Visible-light-driven valorization of biomass intermediates integrated with H₂ production catalyzed by ultrathin Ni/CdS nanosheets. *J Am Chem Soc* 2017; **139**: 15584–7.
52. Xia B, Zhang Y and Shi B *et al.* Photocatalysts for hydrogen evolution coupled with production of value-added chemicals. *Small Methods* 2020; **4**: 2000063.
53. Cha HG and Choi KS. Combined biomass valorization and hydrogen production in a photoelectrochemical cell. *Nat Chem* 2015; **7**: 328–33.
54. Xie SJ, Shen ZB and Deng J *et al.* Visible light-driven C-H activation and C-C coupling of methanol into ethylene glycol. *Nat Commun* 2018; **9**: 1181.
55. Tan CL, Qi MY and Tang ZR *et al.* Cocatalyst decorated ZnIn₂S₄ composites for cooperative alcohol conversion and H₂ evolution. *Appl Catal B* 2021; **298**: 12054.